Watching a signaling protein function in real time via 100-ps time-resolved Laue crystallography

Friedrich Schotte[a], Hyun Sun Cho[a], Ville R. I. Kaila[a], Hironari Kamikubo[b], Naranbaatar Dashdorj[a,1], Eric R. Henry[a], Timothy J. Graber[c], Robert Henning[c], Michael Wulff[d], Gerhard Hummer[a], Mikio Kataoka[b], and Philip A. Anfinrud[a,2]

[a]Laboratory of Chemical Physics, National Institute of Diabetes and Digestive and Kidney Diseases, National Institutes of Health, Bethesda, MD 20892; [b]Graduate School of Materials Science, Nara Institute of Science and Technology, Ikoma, Nara 630-0192, Japan; [c]Center for Advanced Radiation Sources, University of Chicago, Chicago, IL 60637; and [d]European Synchrotron Radiation Facility, Experiments Division, 38043 Grenoble Cedex, France

Edited* by William A. Eaton, National Institute of Diabetes and Digestive and Kidney Diseases, National Institutes of Health, Bethesda, MD, and approved October 4, 2012 (received for review June 26, 2012)

To understand how signaling proteins function, it is crucial to know the time-ordered sequence of events that lead to the signaling state. We recently developed on the BioCARS 14-IDB beamline at the Advanced Photon Source the infrastructure required to characterize structural changes in protein crystals with near-atomic spatial resolution and 150-ps time resolution, and have used this capability to track the reversible photocycle of photoactive yellow protein (PYP) following *trans*-to-*cis* photoisomerization of its *p*-coumaric acid (pCA) chromophore over 10 decades of time. The first of four major intermediates characterized in this study is highly contorted, with the pCA carbonyl rotated nearly 90° out of the plane of the phenolate. A hydrogen bond between the pCA carbonyl and the Cys69 backbone constrains the chromophore in this unusual twisted conformation. Density functional theory calculations confirm that this structure is chemically plausible and corresponds to a strained *cis* intermediate. This unique structure is short-lived (~600 ps), has not been observed in prior cryocrystallography experiments, and is the progenitor of intermediates characterized in previous nanosecond time-resolved Laue crystallography studies. The structural transitions unveiled during the PYP photocycle include *trans*/*cis* isomerization, the breaking and making of hydrogen bonds, formation/relaxation of strain, and gated water penetration into the interior of the protein. This mechanistically detailed, near-atomic resolution description of the complete PYP photocycle provides a framework for understanding signal transduction in proteins, and for assessing and validating theoretical/computational approaches in protein biophysics.

time-resolved X-ray diffraction | photoreceptor | light sensor

To watch a protein function in real time with atomic resolution remains an elusive goal of molecular biophysics. This ability will help remove the mystery regarding how proteins execute their targeted function with remarkable efficiency and extraordinary selectivity, and replace it with a rational, molecular-level description of their reaction pathways. In a step toward this goal, we have developed on the BioCARS 14-IDB beamline at the Advanced Photon Source the infrastructure required to characterize structural changes in protein crystals with near-atomic spatial resolution and 150-ps time resolution, and have used this capability to track the reversible photocycle of a photoactive signaling protein over 10 decades of time, from 100 ps to 1 s.

Signaling proteins give cells the capacity to respond to environmental changes and are crucial to an organism's survival. The messenger to which a cell responds can be chemical, thermal, electrical, or light. Regardless of the source, the messenger typically triggers conformational changes in a signaling protein, whose altered structure leads to a regulatory response in the cell. Although static crystal protein structures provide clues regarding how a signaling protein might accomplish its target function, a complete mechanistic understanding requires knowledge about the sequence of structural changes that lead to the signaling event. When the messenger is chemical, the time required to diffuse to and bind in the active site of a signaling protein is typically far longer than the timescale for protein conformational change. Therefore, chemical-based signaling is not readily amenable to structural studies on fast time-scales. In contrast, when the messenger is light, a laser pulse can be used to trigger a photoreaction at a well-defined instant of time, and the ensuing structural changes can be followed via time-resolved Laue crystallography (1), a pump-probe methodology first demonstrated with nanosecond time resolution (2) and later extended to the picosecond time domain (3).

Light-induced signaling is ubiquitous in nature and includes vision in higher animals, phototropism in plants, and phototaxis in bacteria. For this study, we focused our attention on photoactive yellow protein (PYP), a 14-kDa water-soluble blue-light receptor first discovered in *Halorhodospira halophila* (4), a purple sulfur bacterium that swims away from blue light and toward photosynthetically useful green light (5, 6). Because its action spectrum for negative phototaxis matches the absorbance spectrum of PYP (6), this protein is presumed responsible for the signal that causes this extreme halophile to swim away from photons energetic enough to be genetically harmful. Since its discovery, PYP has served as a useful model system for biophysical studies of signaling proteins (7). The chromophore in PYP is *p*-coumaric acid (pCA), which is covalently linked to the Cys69 residue via a thioester bond (Fig. 1; Movie S1). The C2=C3 double bond is *trans* in the ground state (pG), but upon absorbing a single photon of blue light is converted to *cis* with modest quantum efficiency. This photoisomerization event triggers a sequence of structural changes that involve spectroscopically red-shifted (pR) and blue-shifted (pB) intermediates, the last of which corresponds to the putative signaling state (8–11).

Here, we present a comprehensive description of the structural changes occurring during the PYP photocycle. Based on the structures determined in this work, which are cross-validated with density functional theory (DFT) calculations, we propose a model for the PYP photocycle that is both chemically and mechanistically sensible, and accounts for much of the kinetic complexity observed in prior studies.

Author contributions: F.S., H.S.C., M.K., and P.A.A. designed research; F.S., H.S.C., V.R.I.K., and P.A.A. performed research; F.S., H.S.C., H.K., N.D., T.J.G., R.H., M.W., M.K., and P.A.A. contributed new reagents/analytic tools; F.S., H.S.C., V.R.I.K., E.R.H., G.H., and P.A.A. analyzed data; and P.A.A. wrote the paper.

The authors declare no conflict of interest.

*This Direct Submission article had a prearranged editor.

Freely available online through the PNAS open access option.

Data deposition: The atomic coordinates have been deposited in the Protein Data Bank, www.pdb.org (PDB ID codes 4B9O, 4BBT, 4BBU, and 4BBV).

[1]Present address: Argonne National Laboratory, Argonne, IL 60429.

[2]To whom correspondence should be addressed. E-mail: anfinrud@nih.gov.

This article contains supporting information online at www.pnas.org/lookup/suppl/doi:10.1073/pnas.1210938109/-/DCSupplemental.

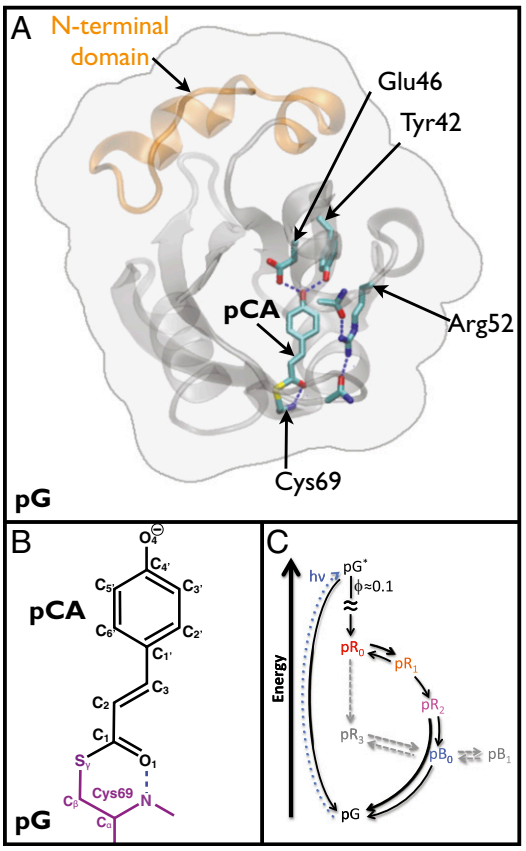

Fig. 1. PYP structure and photocycle. (*A*) Surface rendering (gray) of PYP (PDB ID code 2ZOH) in the pG state with backbone structure (ribbon) and atomic rendering of pCA and its hydrogen-bonding partners. Arrows point to the C2=C3 double bond (pCA) and the Cα atoms of key residues. Hydrogen bonds are indicated with dashed blue lines. Arg52 is stabilized in its "closed" state via hydrogen bonds to the protein backbone. [rendered with VMD (www.ks.uiuc.edu/Research/vmd/)] (*B*) The C2=C3 double bond in pCA is *trans* in its ground state; it absorbs blue light and gives PYP its yellow color. Photoisomerization from *trans* to *cis* triggers the PYP photocycle. (*C*) The PYP photocycle is labeled and color-coded according to intermediates characterized in this study. Intermediates colored gray and connected by dashed lines were not observed in this study, but have been characterized or implicated in prior studies.

Results

Picosecond time-resolved snapshots of the PYP structure were acquired using the pump-probe method (3) (Fig. 2). Briefly, a laser pulse (pump) photoactivates a PYP crystal, after which a suitably delayed X-ray pulse (probe) passes through the crystal and records its diffraction pattern on a 2D detector. Because we use a polychromatic X-ray pulse, we capture thousands of reflections in a single image without having to rotate the crystal. This Laue approach to crystallography boosts substantially the rate at which time-resolved diffraction data can be acquired. The information needed to determine the protein's structure is encoded in the relative intensities of the diffraction spots observed. However, the structural information contained in a single diffraction image is incomplete, requiring repeated measurements at multiple crystal orientations to produce a complete set of data. For this study, diffraction data from 41 orientations using 9 different crystals were combined to produce time-resolved electron density maps at 42 different time-points spanning 10 decades. To mitigate the adverse effects of radiation damage during data collection, very large crystals (12) were used (Fig. S1). Spreading the X-ray dose over the entire length of each crystal maintained high-quality diffraction throughout each of the 41 time-series. To improve the accuracy of the structural information contained in the 1.65-Å resolution Laue diffraction images, we developed an interpolated ratio method for processing the images (*SI Materials and Methods*).

The earliest structural event, the *trans*-to-*cis* photoisomerization of pCA, occurs in ~1–3 ps (13–17) and is too fast to track with 150-ps time resolution. Nevertheless, the structural changes arising from this transition are captured in the 100-ps snapshot shown in Fig. 3 (Movie S2 depicts the structural changes observed throughout the time series). Although structural changes are evident throughout the protein, they are most dramatic in the vicinity of the pCA chromophore. Indeed, the refined pCA structure for the first intermediate detected, which we denote pR_0, is highly contorted with its carbonyl oriented ~90° out of the plane of the phenolate (Fig. 3, curved arrows). This unusual structure has not been trapped in cryotrapping experiments (18–20), and its lifetime is too short to be captured in prior nanosecond time-resolved Laue crystallography experiments (21–23). The driving force for generating this intermediate is the *trans*-to-*cis* photoisomerization of pCA, during which the distance between the Cys69 sulfur and the terminal phenolate oxygen atom (Fig. 1*B*) contracts by ~0.7 Å (Table S1). The pCA chromophore acts like a winch, pulling Glu46 and Tyr42 downward and Cys69 upward (Fig. 3, yellow arrows), thereby shrinking the corresponding Cα–Cα distances between these residues (Table S1) and generating strain in the protein. Remarkably, all three hydrogen bonds between pCA and the protein remain intact, but are clearly strained, as evidenced by longer hydrogen bonding distances to Glu46 and the Cys69 backbone (Table S1). The pR_0 intermediate sets the stage for the transitions that follow and ultimately lead to the long-lived PYP signaling state.

Later in the PYP photocycle, multiple intermediates are simultaneously populated. To determine their structures, we have developed a global data analysis methodology (*SI Materials and Methods*). Starting from a plausible kinetic model, we recover accurate structures of intermediates and accurate rate parameters for interconversion between them. Four intermediates are required to account for our experimental time-resolved electron density maps (Movie S2), the last of which is similar to a structure that has been assigned to a blue-shifted species (22, 24). Hence, we denote these four intermediates pR_0, pR_1, pR_2, and pB_0 (Fig. 4; Movies S3 and S4). Structures similar to pR_1, pR_2, and pB_0 have been reported previously (21, 22, 24, 25), but pR_0 is unique. The simplest possible kinetic model connecting these intermediates is sequential with a reversible pR_0-to-pR_1 transition, and with a pR_2-to-pB_0 transition that short-circuits to the ground pG state approximately half the time (Fig. 4*A*). This simple model accounts for the experimental electron density maps with high fidelity, as illustrated in the calculated vs. experimental color-coded overlays shown in Fig. S2. The ability to assess structurally the validity of a proposed kinetic model, as has been done here (*SI Materials and Methods*), is crucial to understand a protein's mechanism, and is a capability unique to time-resolved crystallography.

Discussion

The pR_0 structure unveiled here corresponds to a highly strained *cis* intermediate that launches the PYP photocycle. The pCA carbonyl in pR_0 is oriented ~90° out of the plane of the phenolate and appears to be locked in this twisted conformation by the hydrogen bond between this carbonyl and the Cys69 backbone nitrogen. This unusual conformation begs the question regarding how this ~90° twist is accommodated among the three dihedral angles between the phenolate and the carbonyl; i.e., is pR_0 a strained *cis* intermediate with the ~90° twist distributed among all three dihedral angles, or is the ~90° twist confined to the C1′–C3=C2–C1 dihedral angle (see notation in Fig. 1*B*) and represents a transition state-like conformation between *trans* and *cis*? With the limited

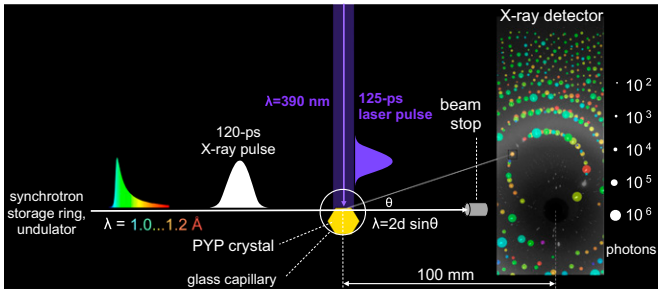

Fig. 2. Pump-probe geometry used to acquire time-resolved diffraction snapshots. The PYP crystal is sealed in a thin-walled glass capillary. Because the laser penetration depth in PYP is shallow, an orthogonal pump-probe geometry is used in which the top edge of the protein crystal is positioned at the top edge of the focused X-ray pulse. This geometry ensures optimal overlap between the laser and X-ray illuminated volumes of the crystal. The protein crystal acts as a monochromator with various line spacings (d) and diffracts different X-ray colors (λ) in different directions (θ) according to Bragg's law (λ = 2d sinθ). Approximately 3,000 spots are found in each time-resolved diffraction image. The spots in this figure are annotated according to integrated photons (spot dimension) and X-ray wavelength (spot color).

resolution of the crystallographic electron density, this question could not be answered unambiguously, because the refined structure depends on the dihedral angle restraints used in the refinement (*SI Materials and Methods*). Hence, we sought further guidance on this issue from DFT calculations (*SI Materials and Methods*). According to the DFT-optimized structure for pR_0, the C1′–C3=C2–C1 dihedral angle is displaced ~30° (Table S1) from its classic *cis* conformation, and should therefore be considered a strained *cis* conformation. To accommodate the full ~90° twist between the phenolate and the carbonyl, other dihedral angles are distorted as well. The X-ray–refined structure is consistent with the DFT-optimized structure provided the variance of the three pCA dihedral angle restraints used in the X-ray refinement are tightened from the default value of ±30° to ±4° (*SI Materials and Methods*). The X-ray–refined and DFT-optimized structures are found to be in excellent agreement for all other intermediates as well (Fig. S4), thereby cross-validating these structures and confirming the plausibility of our pR_0 structure.

Our characterization of pR_0 as a strained *cis* conformation is strongly supported by kinetic arguments as well. The equilibrium established between pR_0 and pR_1 precludes the possibility that pR_0 is a ~90° twisted, transition state-like conformation, because the energy required to break the *cis* double bond in pR_1 and return to pR_0 would be far too high. Moreover, our finding that the quantum yield for producing pR_2 from pR_0 is near unity would be highly unlikely if pR_0 was a transition state-like species, from which return to the *trans* pG ground state should be equally likely. According to DFT energy calculations (*SI Materials and Methods*), pR_0 was found to be similar in energy to pR_1, but pR_2 is ~7 kcal·mol^{-1} lower (Table S1). These results are fully consistent with our observation that the transition between pR_0 and pR_1 is reversible, but the subsequent transition leading to pR_2 is irreversible.

The intermediate structures unveiled in this study permit a detailed examination of mechanistic issues in the PYP photocycle. To facilitate visual comparison of these intermediates, Fig. 4 shows their structures in three different views: color-coded electron density maps of pCA and its immediate surroundings; refined structures for pCA and relevant side chains; and color-coded renderings of protein backbone displacement.

The ultimate fate of pR_0 is dictated by the relative strength of the hydrogen bonds between the chromophore and protein. In wild-type PYP, the hydrogen bond between the Cys69 backbone nitrogen and the pCA carbonyl must be weaker than the phenolate hydrogen bond to Glu46, because the pR_0-to-pR_1 transition involves rupture of the hydrogen bond to Cys69. In the Glu46Gln mutant of PYP, the opposite would be true, and pR_0 (should it exist in this mutant as well) would be expected to transition to the first intermediate recovered (pR_{E46Q}) in prior nanosecond time-resolved Laue studies (26); that structure is similar to pB_0 except the phenolate is hydrogen bonded to Tyr42 instead of Arg52. To be consistent with the nomenclature presented here, we refer to that state as pR_3, because it is further along the pathway to pB_0 than is pR_2.

The pR_0-to-pR_1 transition enables the pCA to assume a planar configuration, which relieves some strain in the protein and the chromophore, but at the cost of breaking a hydrogen bond. According to DFT calculations, the hydrogen bond energy between the pCA carbonyl and the Cys69 backbone is 8.4 kcal·mol^{-1} (Table S1). The pR_0-to-pR_1 transition is reversible, with the two populations quickly establishing an equilibrium that favors pR_1 ~2:1. It follows that the magnitude of the strain energy relieved by the pR_0-to-pR_1 transition must be ~9 kcal·mol^{-1}, ~6 kcal·mol^{-1} of which comes from the pCA chromophore alone (Table S1).

The pR_0-to-pR_1 transition leaves the C2–C1–S–Cβ dihedral angle in a sterically strained *syn* conformation (Table S1). The pR_1-to-pR_2 transition relieves this strain via a dihedral rotation to an *anti* conformation. According to DFT calculations, the strain relieved by the pR_1-to-pR_2 transition is approximately half that relieved by the pR_0-to-pR_1 transition.

The pR_2 state is the most stable red-shifted intermediate observed in this study, and eventually transitions to pB_0 with a time constant of 410 μs. Compared with the first two structural transitions, which involve localized motions, the pR_2-to-pB_0 structural transition is complex, and requires breaking two short (and strong) hydrogen bonds between the phenolate and Tyr42/Glu46, breaking two

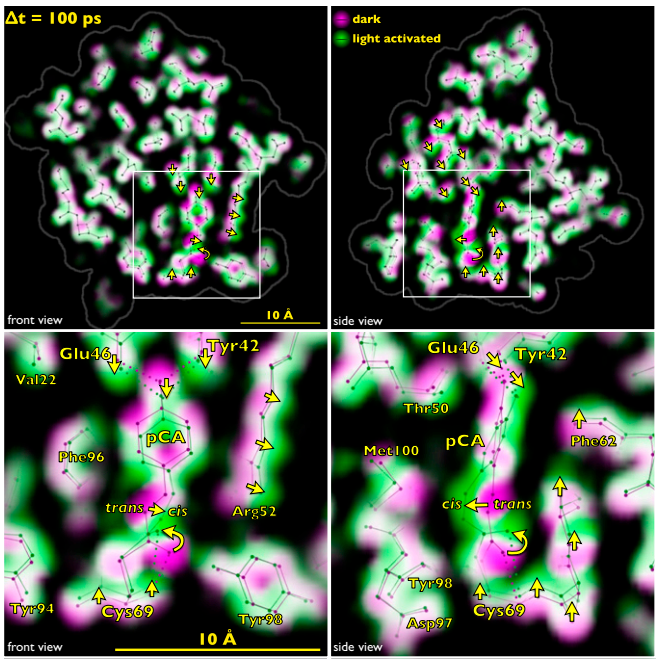

Fig. 3. Front and side views of time-resolved structural changes recorded 100 ps after photoexcitation of PYP. (*Lower*) Expanded, annotated view of *Upper Insets*. The ground-state electron density map is colored magenta, and the 100-ps map is colored green. Where magenta and green overlap, the electron density blends to white. The magenta-to-green color gradient unveils the direction of atomic motion; large-amplitude displacements are indicated with yellow arrows. The stick models correspond to refined structures for the ground state (pG) and the first intermediate (pR_0). Hydrogen bonds to the pCA chromophore are indicated as dotted lines.

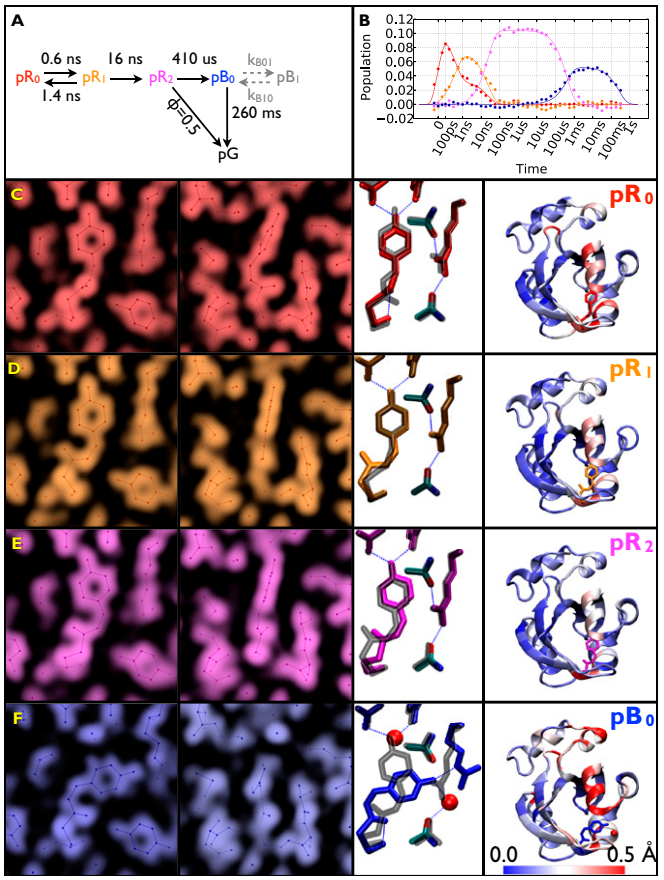

Fig. 4. Time-resolved population of transient intermediates and their structures. (*A*) Kinetic model used to account for structural changes spanning 10 decades; the arrows are labeled with the inverse of the globally refined rate constants. Half the population short-circuits to the ground state during the pR_2-to-pB_0 transition. (*B*) Time-dependent populations of each intermediate in the PYP photocycle: theoretical population predicted by the kinetic model (solid lines) and least-squares contributions from the four electron-density base maps (filled circles). (*C*–*F*) Structures for pR_0, pR_1, pR_2, and pB_0 intermediates. (*Left* and *Center Left*) Electron-density base maps were derived from global analysis and phased according to their refined structures (front and side views; see Fig. S3 for comparison with maps generated using ground-state phases). (*Center Right*) Refined structures of pCA intermediates and their hydrogen-bonding partners. To highlight the structural changes leading to the corresponding intermediate, they are overlaid with a semitransparent structure (gray) of the preceding state. (*Right*) Color-coded rendering of the protein backbone according to Cα displacement relative to pG, as indicated by the scale (rendered with VMD).

hydrogen bonds between Arg52 and the protein backbone, and ~180° rotation of one of the pCA dihedral angles. The transition state for this complex reaction pathway likely imposes significant strain on the C2=C3 bond, which would account for our finding that approximately half the pR_2 population short-circuits to the ground state during this transition.

During the pR_2-to-pB_0 transition, Arg52 switches to an "open" conformation that exposes the pCA phenolate to water (Fig. S5) and facilitates its protonation, an event that triggers a blue shift of the pCA absorbance spectrum (27). Indeed, the pB_0 intermediate has a water molecule hydrogen bonded to the phenolate and the protein backbone. The open Arg52 conformation also facilitates penetration of a water molecule into the pCA cavity, which is stabilized by hydrogen bonds to Tyr42 and Glu46. Because this water molecule must escape before the pB_0 state can revert to the pG state, its presence likely prolongs the lifetime of the pB_0 state. Note that the pB_0 state reported here does not have the same global structure as that produced in solution, where the N-terminal domain is free to move beyond the constraints imposed by crystal packing. In our kinetic model, the crystal-inaccessible "signaling" intermediate, in which the N-terminal domain is believed to be partially unfolded (28–30), is denoted pB_1.

Changes in backbone displacement during the PYP photocycle are clearly evident in the color-coded (blue-white-red) ribbon structures of Fig. 4. These maps show a diminution of red coloration as the photocycle advances from pR_0 to pR_1 to pR_2, indicating relaxation of protein strain. The pR_2-to-pB_0 transition, however, exhibits large amplitude, globally distributed displacements of the protein backbone. Although the putative pB_1 signaling state is not achieved in the protein crystal, substantial motion in the N-terminal domain is detected during the pR_2-to-pB_0 transition, which is consistent with this region being implicated in the formation of the signaling state.

According to DFT energy calculations (*SI Materials and Methods*), the earliest intermediates store approximately one-third of the photon energy in the form of protein strain, which provides ample excess energy to drive the photocycle to the signaling state and back down to the ground state. The driving force for the final pB_0-to-pG transition should be sufficiently high to avoid thermal activation of pB_0. This driving force appears to reside primarily in intramolecular strain in the pCA chromophore and the relative strength of its hydrogen-bonding interactions. The pB_0-to-pG transition not only relieves the strain imposed by the *cis* conformation of pCA, but also exchanges two weaker hydrogen bonds for two short, strong hydrogen bonds. Due to the energetic cost of reversing this transformation, thermal activation of the pG state is an improbable event, as desired for a photoactive protein.

The lifetime of a signaling state must be sufficiently long for an organism to recognize and act upon its message, but not too long to remain stuck in the "on" state. *H. halophila* responds to changes in blue-light intensity in ~0.5 s (6), which is of the same order of magnitude as the 0.26-s pB_0 lifetime reported here. This lifetime is determined by the height of the activation barrier for ground-state recovery, which is likely dominated by the energy required to break the C2=C3 *cis* bond. Thus, the pCA prosthetic group, which is capable of *trans*-to-*cis* photoisomerization, provides an energetically and structurally attractive framework for inducing and sustaining a long-lived signaling state in PYP.

The PYP photocycle found here differs from what was reported in earlier nanosecond time-resolved Laue crystallography studies (22, 23). Those studies lacked the time resolution to capture pR_0, but managed to characterize pR_1, which was believed to bifurcate to both pR_2 and pR_3 with pR_2 favored 3:2. If pR_3 is present in this study, its population is too small to be characterized. Moreover, those studies did not report water penetration into the pCA cavity (22, 23), except at pH 4 (23), and found the ground-state recovery from pB to be biexponential, with most of the population converting to pG on a 10- to 20-ms time scale (22, 23). Here, the ground-state recovery from pB_0 is exponential with a much longer, 260-ms time constant. The differences between this and earlier studies cannot be ascribed solely to improvements in data quality and the data analysis procedure, but appear to be due to differences in sample preparation. Extreme halophiles tolerate a high intracellular NaCl concentration. For example, *Halobacterium salinarum* grown in 4 M NaCl has been shown to have an intracellular NaCl concentration of 3.6 M (31). Nevertheless, most studies of PYP have been performed under conditions with relatively little or no NaCl present. In contrast, this study was carried out with $P6_3$ PYP crystals grown with 1.1 M NaCl in D_2O, pD 9.0. Under these conditions, which are arguably more physiologically relevant compared with prior crystallography studies, the PYP photocycle can be described by a simple, sequential model with four well-defined structural intermediates, whose lifetimes correlate favorably with those measured in solution studies. Similar results have been

obtained at pH 7.0, demonstrating that the differences between this and earlier work are not due to pH or hydrogen/deuterium isotope differences. Evidently, the presence of 1.1 M NaCl mediates penetration of water into the pCA cavity, which accounts for the long-lived pB_0 state reported here. Interestingly, the longer-lived pB population reported in earlier studies (22, 23) has a lifetime similar to what we find here, and may arise from water occupancy in the pCA cavity that is too low to be detected in the maps.

The intermediates found in this work provide a structural framework for interpreting the wealth of prior time-resolved spectroscopic studies of PYP in solution, a few examples of which are presented here. (*i*) Transient optical absorbance spectra of PYP in solution (13, 14) unveiled a short-lived intermediate peaked at ∼510 nm that relaxed to a longer-lived feature peaked at ∼460 nm. We associate the short-lived 510-nm intermediate with pR_0 and the longer-lived 460-nm intermediate with pR_1 and pR_2, which are similar in structure and would be expected to have similar optical absorbance spectra. The lifetimes reported for the short-lived intermediate, 3.0 ns for $I_0^{\ddagger}$ (13) and 1.3 ns for PYP_B (14), are longer than the 600-ps lifetime we find for pR_0; however, the lifetime recovered in this study is expected to be shortened by the unavoidable <30 K adiabatic temperature jump that arises when photoactivating PYP crystals with the laser pulses used in this study. (*ii*) Prior studies uncovered an equilibrium between red- and blue-shifted intermediates (32, 33). We find no evidence for an equilibrium between pR_2 and pB_0, and would not expect it for reasons already discussed; however, if pR_3 were formed in solution, it would be expected to coexist in equilibrium with pB_0. A mixture of pR_2 and pR_3 would also account for the biexponential kinetics reported for the conversion of pR to pB (8). (*iii*) Hendriks et al. (32) characterized the PYP photocycle over a wide range of pH and pD, and in table 1 of ref. 30 reported relaxation times at pH 8.1 and pH 9.55, whose averages are remarkably similar to what we find in PYP crystals at pD 9.0: 420 (410) μs for pR to pB, and 220 (260) ms for pB to pG (our determinations in parentheses). The fact that the pR and pB lifetimes in crystals grown in ∼1.1 M NaCl are similar to those found in solution at a similar pH/pD (32) suggests that the pCA photocycle in our crystals is authentic, and is only loosely coupled to the large-amplitude displacement that accompanies the putative pB_0-to-pB_1 signaling transition.

The time-resolved structural evolution presented here, spanning 10 decades, unveil a simple, step-wise structural progression of PYP conformations toward a long-lived pB_0 state, with each transition characterized at an unprecedented level of detail. The highly contorted structure of the pR_0 state is unique, and provides a visual clue regarding the conformational gymnastics that must accompany *trans*-to-*cis* isomerization in a highly constrained protein environment. These results illustrate how a protein can use hydrogen bonding networks, gated water penetration, and strain to steer the direction of structural transitions in a fashion that facilitates its target function. The time-resolved methodology developed for this study of PYP is, in principle, applicable to any other crystallizable protein whose function can be directly or indirectly triggered with a pulse of light. Indeed, it may prove possible to extend this capability to the study of enzymes, and literally watch an enzyme as it functions in real time with near-atomic spatial resolution. By capturing the structure and temporal evolution of key reaction intermediates, picosecond time-resolved Laue crystallography can provide an unprecedented view into the relations between protein structure, dynamics, and function. Such detailed information is crucial to properly assess the validity of theoretical and computational approaches in biophysics. By combining incisive experiments and theory, we move closer to resolving reaction pathways that are at the heart of biological functions.

Materials and Methods

Data reduction and analysis methodologies are described in *SI Materials and Methods*, which includes Figs. S6–S10. Data collection statistics are found in Table S2, and refinement statistics are found in Table S3.

Crystal Preparation. Wild-type PYP apoprotein was overexpressed in *Escherichia coli*, isolated, and then reconstituted with pCA anhydride in 4 M urea buffer (34). The holoprotein was purified by column chromatography (DEAE Sepharose CL6B; Amersham Biosciences) several times until the optical purity index (absorbance 277 nm/absorbance λ_{max}) became <0.44. Large $P6_3$ crystals of PYP were grown from microseeds via the hanging-drop vapor diffusion method (12). The crystallization hanging-drop solution contained 24 mg·mL^{-1} PYP, 2.2 M ammonium sulfate, 1.0 M sodium chloride, and 20 mM sodium phosphate. The reservoir solution contained 2.5 M ammonium sulfate and 1.1–1.2 M sodium chloride, and was maintained at 293 K. The crystallization buffers were prepared with 99.9% heavy water (Aldrich) and titrated to pD 9.0. This method produced high-quality crystals ∼2 mm in length. The crystals were mounted in 1.5-mm diameter glass capillaries whose inner wall was texturized by bonding thin shards of crushed glass to its surface with polyvinyl formyl. Crystals mounted on the roughened surface are far less prone to slippage during data collection, which can be problematic due to the shock wave generated in the crystal after an intense, short duration laser pulse is absorbed and suddenly heats its surface.

X-Ray Source. The data reported here were acquired on the BioCARS 14-IDB beamline (35) at the Advanced Photon Source in March 2011 when the ring was operated in hybrid mode. During this run, 12-keV polychromatic (5% FWHM), 120-ps–duration X-ray pulses with nearly 3×10^{10} photons were focused to an 80×40 (horizontal by vertical) μm^2 spot at the sample position.

Laser Source. The picosecond laser system used in this study employs a Spectra Physics Spitfire Pro designed to produce 5 mJ 1.2-ps optical pulses at 780 nm. To produce ∼120-ps pulses, we used a 0.8-nm band-pass interference filter to bandwidth limit the seed pulses delivered to the amplifier pulse stretcher, and then bypassed the grating pulse compressor by inserting a large right-angle prism into the optical layout of the Spitfire Pro. The laser pulse was frequency doubled to 390 nm in a type I β-barium borate nonlinear crystal custom-designed for these pulse characteristics. The 390-nm laser pulses were beam expanded and transported from the laser hutch to the X-ray hutch where beam-conditioning optics spatially filtered the beam and focused it to a 0.12×0.6 mm elliptical spot with the long axis aligned along the propagation direction of the X-ray beam. The beam conditioning optics arrangement includes a variable attenuator to control the pulse energy and a Berek polarization compensator to set the laser polarization.

PYP Photoactivation. The peak absorbance of the pCA chromophore in $P6_3$ crystals (447 nm) is very strong and birefringent (71.4/407.1 mm^{-1} ∥/⊥ to the *c*-axis) (36). To match the laser penetration depth to the 40-μm vertical X-ray beam size, the laser must be tuned well to the red or blue edge of the ground-state absorbance. Because the first intermediate in the PYP photocycle has a red-shifted absorbance spectrum, it is preferable to photoactivate PYP on the blue edge. Moreover, it is preferable to photoactivate the crystal with laser pulses polarized parallel to the *c*-axis, which maximizes the laser penetration depth and reduces the strong depth-dependent gradient that would arise from using either circularly polarized or unpolarized laser pulses.

The laser system and beam conditioning optics were set up to deliver intense (3.5 mJ·mm^{-2}), polarized (|| to *c*-axis), stretched (125-ps) optical pulses tuned to the blue edge of the ground-state absorption spectrum (390 nm). Under these conditions, the laser penetration depth is only 28 μm (1/e). Use of a stretched, intense optical pulse to photoactivate the PYP crystal boosts the *trans*-to-*cis* isomerization yield by providing the pCA chromophore multiple opportunities to isomerize during the optical pulse.

To ensure optimal overlap between the laser and X-ray pulses, it is crucial to align the top edge of the crystal with the top edge of the X-ray pulse (Fig. 2). To accomplish this feat, we developed an edge-finder routine that scans the crystal vertically through an attenuated X-ray beam while acquiring single-shot diffraction images. The extrapolated edge of the crystal is deduced from the integrated spot intensities, and the crystal is positioned to align its top edge with that of the X-ray beam. With this approach, the photoisomerization yield within the volume probed by X-rays was ∼10%.

During data collection, the crystals were chilled to 288 K with a nitrogen-gas cooling stream. The energy deposited in the protein crystal by the laser

pulse triggers an adiabatic temperature jump that is largest at the protein surface and decreases as a function of depth. Given the conditions used in this study, the magnitude of the temperature jump decreases from ~30 K to 7 K across the 40-μm vertical cross-section of the X-ray beam. Because the thermal conductivity in a protein crystal is quite high and its heat capacity large, the temperature in the X-ray–illuminated volume of the crystal rapidly cools to the cooling-stream temperature. Consequently, the early-time dynamics are recorded at an elevated temperature, which would be expected to shorten the lifetimes of the earliest detected intermediates, whereas the long-time dynamics are recorded at a near-normal temperature. In contrast, the protein concentration in time-resolved optical spectroscopy experiments is comparatively low, so the adiabatic temperature jump in those studies is negligible.

Data Collection Protocol. Time-resolved diffraction images were acquired at 42 time delays spanning 10 decades, with four time points per decade. Interleaved between these time delays were twelve −1-ns reference images in which the X-ray pulse arrived 1 ns ahead of the laser pulse. A complete time series was acquired at each of six or more orientations per crystal on nine crystals. To improve the signal-to-noise ratio of each diffraction image, five consecutive pump-probe shots were integrated on the mar165 CCD detector before readout. The crystal was translated ~250 μm along its long axis after each laser shot to avoid buildup of long-lived states. The time required for crystal translation and detector readout averaged 13 s per image. The starting position for each time point in the series was offset horizontally to uniformly distribute the radiation dose over the entire length of the protein crystal. This approach minimized the adverse effects of radiation damage and preserved high-quality diffraction throughout the entire time series.

ACKNOWLEDGMENTS. We thank Drs. Keith Moffat, Vukica Srajer, Hyocherl Ihee, and Yang Ouk Jung for their contributions to earlier, collaborative time-resolved Laue studies of PYP; Bernard Howder, Jr., for machining many of the components required for this study; the Biowulf cluster at the National Institutes of Health (NIH) for computer time; and the Advanced Photon Source undulator group for reconfiguring and installing two short-period undulators on the 14-IDB BioCARS beamline. Use of the BioCARS Sector 14 was supported by National Center for Research Resources Grant 5P41RR007707 and National Institute of General Medical Sciences Grant 8P41GM103543 from NIH. Use of the Advanced Photon Source, an Office of Science User Facility operated for the US Department of Energy (DOE) Office of Science by Argonne National Laboratory, was supported by US DOE Contract DE-AC02-06CH11357. The time-resolved setup at Sector 14 was funded in part through collaboration with P.A.A. This research was supported by the Intramural Research Program of the National Institute of Diabetes and Digestive and Kidney Diseases, NIH. V.R.I.K. is the recipient of a European Molecular Biology Organization Long-Term Fellowship. VMD was developed by the Theoretical and Computational Biophysics Group in the Beckman Institute for Advanced Science and Technology at the University of Illinois at Urbana-Champaign.

1. Eaton WA, Henry ER, Hofrichter J (1996) Nanosecond crystallographic snapshots of protein structural changes. *Science* 274(5293):1631–1632.
2. Srajer V, et al. (1996) Photolysis of the carbon monoxide complex of myoglobin: Nanosecond time-resolved crystallography. *Science* 274(5293):1726–1729.
3. Schotte F, et al. (2003) Watching a protein as it functions with 150-ps time-resolved x-ray crystallography. *Science* 300(5627):1944–1947.
4. Meyer TE (1985) Isolation and characterization of soluble cytochromes, ferredoxins and other chromophoric proteins from the halophilic phototrophic bacterium *Ectothiorhodospira halophila*. *Biochim Biophys Acta* 806(1):175–183.
5. Hustede E, Liebergesell M, Schlegel HG (1989) The photophobic response of various sulfur and nonsulfur purple bacteria. *Photochem Photobiol* 50(6):809–815.
6. Sprenger WW, Hoff WD, Armitage JP, Hellingwerf KJ (1993) The eubacterium *Ectothiorhodospira halophila* is negatively phototactic, with a wavelength dependence that fits the absorption spectrum of the photoactive yellow protein. *J Bacteriol* 175(10): 3096–3104.
7. Hellingwerf KJ, Hendriks J, Gensch T (2003) Photoactive yellow protein, a new type of photoreceptor protein: Will this "yellow lab" bring us where we want to go? *J Phys Chem A* 107(8):1082–1094.
8. Meyer TE, Yakali E, Cusanovich MA, Tollin G (1987) Properties of a water-soluble, yellow protein isolated from a halophilic phototrophic bacterium that has photochemical activity analogous to sensory rhodopsin. *Biochemistry* 26(2):418–423.
9. Meyer TE, Tollin G, Hazzard JH, Cusanovich MA (1989) Photoactive yellow protein from the purple phototrophic bacterium, *Ectothiorhodospira halophila*. Quantum yield of photobleaching and effects of temperature, alcohols, glycerol, and sucrose on kinetics of photobleaching and recovery. *Biophys J* 56(3):559–564.
10. Meyer TE, Tollin G, Causgrove TP, Cheng P, Blankenship RE (1991) Picosecond decay kinetics and quantum yield of fluorescence of the photoactive yellow protein from the halophilic purple phototrophic bacterium, *Ectothiorhodospira halophila*. *Biophys J* 59(5):988–991.
11. Hoff WD, et al. (1994) Measurement and global analysis of the absorbance changes in the photocycle of the photoactive yellow protein from *Ectothiorhodospira halophila*. *Biophys J* 67(4):1691–1705.
12. Yamaguchi S, et al. (2007) Preparation of large crystals of photoactive yellow protein for neutron diffraction and high resolution crystal structure analysis. *Photochem Photobiol* 83(2):336–338.
13. Ujj L, et al. (1998) New photocycle intermediates in the photoactive yellow protein from *Ectothiorhodospira halophila*: Picosecond transient absorption spectroscopy. *Biophys J* 75(1):406–412.
14. Imamoto Y, Kataoka M, Tokunaga F, Asahi T, Masuhara H (2001) Primary photoreaction of photoactive yellow protein studied by subpicosecond-nanosecond spectroscopy. *Biochemistry* 40(20):6047–6052.
15. Groot ML, et al. (2003) Initial steps of signal generation in photoactive yellow protein revealed with femtosecond mid-infrared spectroscopy. *Biochemistry* 42(34):10054–10059.
16. van Wilderen LJGW, et al. (2006) Ultrafast infrared spectroscopy reveals a key step for successful entry into the photocycle for photoactive yellow protein. *Proc Natl Acad Sci USA* 103(41):15050–15055.
17. Larsen DS, et al. (2004) Incoherent manipulation of the photoactive yellow protein photocycle with dispersed pump-dump-probe spectroscopy. *Biophys J* 87(3):1858–1872.
18. Genick UK, Soltis SM, Kuhn P, Canestrelli IL, Getzoff ED (1998) Structure at 0.85 A resolution of an early protein photocycle intermediate. *Nature* 392(6672):206–209.
19. Anderson S, Srajer V, Moffat K (2004) Structural heterogeneity of cryotrapped intermediates in the bacterial blue light photoreceptor, photoactive yellow protein. *Photochem Photobiol* 80(1):7–14.
20. Kort R, Hellingwerf KJ, Ravelli RBG (2004) Initial events in the photocycle of photoactive yellow protein. *J Biol Chem* 279(25):26417–26424.
21. Perman B, et al. (1998) Energy transduction on the nanosecond time scale: Early structural events in a xanthopsin photocycle. *Science* 279(5358):1946–1950.
22. Ihee H, et al. (2005) Visualizing reaction pathways in photoactive yellow protein from nanoseconds to seconds. *Proc Natl Acad Sci USA* 102(20):7145–7150.
23. Tripathi S, Srajer V, Purwar N, Henning R, Schmidt M (2012) pH dependence of the photoactive yellow protein photocycle investigated by time-resolved crystallography. *Biophys J* 102(2):325–332.
24. Genick UK, et al. (1997) Structure of a protein photocycle intermediate by millisecond time-resolved crystallography. *Science* 275(5305):1471–1475.
25. Anderson S, Crosson S, Moffat K (2004) Short hydrogen bonds in photoactive yellow protein. *Acta Crystallogr D Biol Crystallogr* 60(Pt 6):1008–1016.
26. Rajagopal S, et al. (2005) A structural pathway for signaling in the E46Q mutant of photoactive yellow protein. *Structure* 13(1):55–63.
27. Hendriks J, Hoff WD, Crielaard W, Hellingwerf KJ (1999) Protonation/deprotonation reactions triggered by photoactivation of photoactive yellow protein from *Ectothiorhodospira halophila*. *J Biol Chem* 274(25):17655–17660.
28. van der Horst MA, van Stokkum IH, Crielaard W, Hellingwerf KJ (2001) The role of the N-terminal domain of photoactive yellow protein in the transient partial unfolding during signalling state formation. *FEBS Lett* 497(1):26–30.
29. Harigai M, et al. (2001) Amino acids in the N-terminal region regulate the photocycle of photoactive yellow protein. *J Biochem* 130(1):51–56.
30. Harigai M, Imamoto Y, Kamikubo H, Yamazaki Y, Kataoka M (2003) Role of an N-terminal loop in the secondary structural change of photoactive yellow protein. *Biochemistry* 42(47):13893–13900.
31. Christian JH, Waltho JA (1962) Solute concentrations within cells of halophilic and non-halophilic bacteria. *Biochim Biophys Acta* 65:506–508.
32. Hendriks J, van Stokkum IHM, Hellingwerf KJ (2003) Deuterium isotope effects in the photocycle transitions of the photoactive yellow protein. *Biophys J* 84(2 Pt 1): 1180–1191.
33. Borucki B, et al. (2003) pH Dependence of the photocycle kinetics of the E46Q mutant of photoactive yellow protein: Protonation equilibrium between I1 and I2 intermediates, chromophore deprotonation by hydroxyl uptake, and protonation relaxation of the dark state. *Biochemistry* 42(29):8780–8790.
34. Mihara K, Hisatomi O, Imamoto Y, Kataoka M, Tokunaga F (1997) Functional expression and site-directed mutagenesis of photoactive yellow protein. *J Biochem* 121(5):876–880.
35. Graber T, et al. (2011) BioCARS: A synchrotron resource for time-resolved X-ray science. *J Synchrotron Radiat* 18(Pt 4):658–670.
36. Ng K, Getzoff ED, Moffat K (1995) Optical studies of a bacterial photoreceptor protein, photoactive yellow protein, in single crystals. *Biochemistry* 34(3):879–890.

Supporting Information

Schotte et al. 10.1073/pnas.1210938109

SI Materials and Methods

Interpolated Ratio Method. The diffraction spots in each image of a time series were indexed and integrated, and the crystal orientation refined. The structural information we seek is encoded in pump-induced changes of the spot intensities, whose absolute amplitude depends on crystal volume, crystal orientation, the X-ray wavelength exciting the corresponding Bragg reflections, and the X-ray intensity. To minimize systematic sources of error that can arise when merging diffraction data acquired at different orientations on different crystals, we use a variation of the ratio method developed by Coppens et al. (1) and Vorontsov et al. (2). That method is based upon back-to-back diffraction images acquired with (ON) and without (OFF) a laser pump pulse. By merging I_{ON}/I_{OFF} ratios of integrated spot intensities for each indexed reflection (R_{hkl}), instead of intensity differences (ΔI_{hkl}), errors arising from image scaling and wavelength normalization are avoided. After merging, the ratios can be converted to structure factor amplitude differences by multiplying each ground-state structure factor amplitude by its corresponding $R_{hkl} - 1$.

Instead of using I_{ON}/I_{OFF}, we use I_{ON}/I_{REF} where I_{REF} is computed by cubic spline interpolation between integrated spot intensities from 12 reference images interleaved among the 42 time delays (Fig. S6). From a data-collection strategy point of view, this interpolated ratio method is more efficient because it requires fewer total diffraction images in each time series. For this study, the reference images correspond to −1-ns time points, i.e., the X-ray pulse arrives 1 ns in advance of the laser pulse.

Laser-triggered structural changes in the protein crystal cause some reflections to get brighter and some dimmer, with the average ratio for each image expected to be 1. However, the weighted average of all ratios R_{hkl} computed in a single image is generally found to be less than 1 due to laser-induced strain in the crystal, which reduces its diffraction efficiency (Fig. S7). The weights used in the weighted average are derived from the experimental uncertainty of R_{hkl} according to $w = 1/\sigma_R^2$; before processing the data further, they are put on a common scale by rescaling the ratios so the weighted average for each time point is 1.

Excitation Degree Scaling. If an R_{hkl} is sensitive to laser-induced structural changes, it will deviate from unity by a factor that is proportional to the excitation degree, which can vary due to differences in the laser pump fluence. The R_{hkl} can be corrected for differences in the excitation degree by a simple scaling procedure using

$$R^s_{hkl} = 1 + s_i(R_{hkl} - 1)$$

where s_i is the scale factor corresponding to time series i. We find the set of s_i that minimizes the differences between redundant R^s_{hkl} acquired at different orientations and with different crystals.

Outlier Rejection. Provided the crystal orientation remains stable through the time series, the time dependence of R_{hkl} is expected to evolve smoothly and monotonically. However, laser excitation launches an acoustic shock wave in the protein crystal, and occasionally causes the crystal to slip or twitch in the capillary, an event that generates a discontinuity in R_{hkl}. Time series that suffer from sudden changes in crystal orientation are excluded from the merging step.

R_{hkl} Merging. Instead of merging intensities time-point by time-point, we merge complete R^s_{hkl} time series with the weight for each series computed from the average uncertainty across the series, i.e., $w = 1/\sigma_R^2$. If the crystal orientation slips during acquisition of a time series, that time series is rejected. This vector-based approach to merging ensures that the completeness and weights used to calculate the electron density maps are the same throughout each time series, thereby improving the accuracy of our electron density maps and our refined kinetic rate constants.

Time-Dependent Electron Density Map Generation. The merged R^s_{hkl} vectors characterize the time-dependent change in scattering power for each observed reflection. The R^s_{hkl} are converted to structure factor amplitude differences using ground-state structure factor amplitudes calculated from a high-resolution (1.25 Å) room-temperature structure of WT photoactive yellow protein (PYP) acquired under similar conditions (PDB ID code 2ZOH). This high-resolution structure is also used to phase the experimental time-dependent structure factor amplitudes, whose Fourier transform produced the electron density maps used to generate Movie S2 and the 100-ps time-resolved snapshots shown in Fig. 3.

Real-Space Global Analysis Method. The time-resolved electron-density difference maps used to produce each frame in Movie S2 have contributions from one or more intermediates. To extract electron-density difference maps for the intermediates represented in the experimental data and determine the kinetics for their interconversion, we developed a real-space global analysis approach in which the kinetic rate parameters used to define the time-dependent populations of putative intermediates are refined by nonlinear least squares, whereas the electron-density difference maps for the corresponding intermediates are determined by linear least squares. We start with a plausible kinetic model (Fig. 1*C*) whose corresponding rate equations account not only for the first-order processes for structure interconversion, but also for the rate of photoactivation, which depends on the instrument response function, i.e., the convolution of the laser and X-ray pulses. The ability to properly account for the experimental instrument response function is crucial for accurate determination of lifetimes approaching its width, which in this case is ∼150 ps.

We recover "base" electron-density difference maps for the intermediates, $\Delta\boldsymbol{\rho}_b$, by finding the least-squares solution to

$$\Delta\boldsymbol{\rho}_t \cong \mathbf{P}_t \Delta\boldsymbol{\rho}_b,$$

where $\Delta\boldsymbol{\rho}_t$ is a $42 \times n$ matrix representing 42 observed time-resolved electron-density difference maps, $\mathbf{P}_t$ is a 42×4 matrix representing the time-dependent populations for each of four intermediates in our kinetic model (Fig. 4*B*), and $\Delta\boldsymbol{\rho}_b$ is a $4 \times n$ matrix representing four base electron-density difference maps, one for each intermediate. The parameters in our kinetic model are refined iteratively using the Marquardt–Levenberg algorithm, which minimizes the residual found when solving this linear equation. Because structural changes are largest in the vicinity of the *p*-coumaric acid (pCA) chromophore, the least-squares refinement was confined to n = 4,983 voxels found within 2.5 Å of the chromophore. This restricted-range approach enhances the sensitivity of the kinetic model to structural dynamics occurring in the chromophore region, and improves the accuracy of its refined parameters. Once the population matrix is known, we solve this linear equation using all voxels in the unit cell (n = 2,689,600) and generate complete base maps.

Note that this global analysis method could have been applied to structure factors in reciprocal space rather than electron density voxels in real space. However, it is not possible to define a region of interest in reciprocal space, so the accuracy of the refined kinetic rate parameters would be poorer than can be achieved with our real-space approach.

Not all parameters in our kinetic model are refinable by least-squares methods and must be specified independently. For example, the photoproduct yield affects the initial pR_0 population, and incorrect assumptions about this yield lead to contamination of its base map with electron density from the ground state. This contamination was found to be negligible when the photoproduct yield was set to 10%. When the photoproduct yield of pB_0 was assumed to be 10% as well, the electron density map assigned to pB_0 appeared to be a 50:50 mixture of the ground and pB_0 states (Fig. S8*A*); when set to 5%, the electron density map for pB_0 is well described by a single structure (Fig. S8*B*). Hence, ~50% of the pR_2 population short-circuits to the ground state during the pR_2-to-pB_0 transition, and our kinetic model was modified accordingly.

Although our real-space global analysis approach recovers electron density maps for all intermediates in the model, the maps generated are not guaranteed to be chemically sensible. Therefore, structure refinement is required to assess and validate the proposed model.

Structure Refinement. Atomic structures for each intermediate in the model were refined in reciprocal space using phenix.refine, a program that implements the restrained maximum-likelihood method (3). This program requires as input structure factor amplitudes and their estimated uncertainties. To generate $\Delta\mathbf{F}_b$, the base structure factor amplitude differences, we Fourier-transformed $\Delta\boldsymbol{\rho}_b$, the complete base difference density maps generated by our global analysis. To generate $\boldsymbol{\sigma}^2(\Delta F_b)$, the variance for the base structure factor amplitude differences, we used linear algebra to propagate the experimental variances for $\boldsymbol{\sigma}^2(\Delta F_t)$, which are derived from photon-counting statistics.

To mitigate the effects of modeling error, we used the method of difference refinement (4), using as input for the refinement program the calculated ground-state structure factors, $\mathbf{F}_c$, plus our structure factor amplitude differences, $\Delta\mathbf{F}_b$ (intermediate minus ground state):

$$\mathbf{F}_b = \mathbf{F}_c + \Delta\mathbf{F}_b.$$

The restraints needed for the pCA chromophore are not included in the restraints library of the PHENIX package, and were instead generated by the program eLBOW (Electronic Ligand Bond Builder and Optimization Workbench), a utility distributed with PHENIX. The eLBOW-generated restraints were used with one exception: the pCA dihedral bond angle restraints were set to 0/180 ± 4°, as opposed to eLBOW default values of 0/180 ± 30°. The default variance proved far too generous, and allowed the default bond angle restraints (120 ± 3°) to dictate the structure. Indeed, the default restraints produced a structure in which the ~90° twist between the phenolate and the carbonyl was absorbed almost entirely by the C1′–C3 = C2–C1 dihedral angle, in stark contrast to DFT calculations, which distribute the twist among all three dihedral angles between the phenolate and the carbonyl. For our refinement, the three dihedral bond angles were assigned the same restraints, a choice justified by the fact that the pCA absorbance is red-shifted in the pR_0 state, and must therefore remain well-conjugated.

The crystallographic data and data collection statistics are summarized in Table S2, and the refinement statistics are summarized in Table S3. The signal-to-noise ratio (S/N) of the electron density maps for each intermediate reflects the number of images in which the intermediate is represented, as well as its relative population. Because the photoproduct yield is ~10%, the S/N of the intermediates is ~10-fold poorer than that for the ground state. However, these intermediates are represented in numerous frames of the time series, which improves their S/N. Note that the S/N for pR_0 is poorer than that for pR_1 and pR_2, reflecting the smaller number of frames in which this intermediate is represented.

Kinetic Model Validation. The validity of a kinetic model can be assessed by comparing the experimental electron density maps with those computed from the refined atomic coordinates for each intermediate. If differences between the experimental and computed electron density maps rise above the noise and vary systematically in space, the kinetic model is deemed invalid and needs to be modified accordingly. The aim is to find a kinetic model that accounts for the time-resolved electron density maps with the fewest possible intermediates and rate parameters, i.e., Occam's razor. The fit residuals visualized in Fig. S2 demonstrate that the kinetic model used in this study reproduces the experimentally determined time-resolved structures with high fidelity. This validation test failed for the first kinetic model tried: when the pR_0-to-pR_1 transition was considered irreversible, the residuals between the calculated and experimental electron densities for pR_1 revealed significant contamination by pR_0 (Fig. S9). After making the pR_0-to-pR_1 transition reversible, this contamination disappeared (Fig. S10).

Density Functional Theory Calculations. The molecular structures of all experimentally observed states (pG, pR_0, pR_1, pR_2, and pB_0) were optimized using dispersion-corrected density functional theory, D-BP86 (5–8), with the Karlsruhe split valence polarized basis set, def2-SVP (9). Using starting coordinates from the X-ray–refined structures of pR_0, pR_1, and pR_2, density functional theory (DFT) optimization of the pCA chromophore in vacuum converged to the same *cis* state. Clearly, interactions with the protein are required to stabilize the intermediates observed in PYP. The protein cavity in which pCA resides is surrounded by 12 residues (Y42, E46, T50, R52, F62, V66, A67, P68, C69, T70, F96, and M100). A quantum chemical model was constructed from pCA and these residues, with Tyr42, Glu46, and Arg52 protonated. The pCA was deprotonated in all states except pB_0 (see below). To trim the size of the model, residues whose backbone atoms are not involved in hydrogen bonding networks were terminated at the Cβ position. This protein model, which is comprised of 176 atoms (192 atoms in pB_0), was optimized with the backbone atoms constrained to their X-ray–refined coordinates. All DFT structures were found to be in excellent agreement with the X-ray structures (Fig. S4), suggesting that the protonation-state assignments are correct. Indeed, protonation of pCA in the pR states, or deprotonation of pCA in the pB_0 state, led to large discrepancies between the X-ray and DFT structures.

DFT calculations were also carried out to evaluate the relative quantum chemical energies for each pR state, relevant hydrogen bond energies, as well as chromophore strain energy. The chromophore strain energy was calculated as the difference between the energy of the chromophore in its protein- and vacuum-relaxed conformations. For these single-point energy calculations, we used Becke's three-parameter functional with empirical dispersion correction, D-B3LYP (7, 8, 10, 11) and a triple-ζ basis set augmented with polarization functions, def2-TZVP (12). Solvation effects were modeled using COSMO (13) with the dielectric constant set to 4. All quantum chemical calculations were performed using TURBOMOLE version 6.3 (14).

1. Coppens P, et al. (2009) The RATIO method for time-resolved Laue crystallography. *J Synchrotron Radiat* 16(Pt 2):226–230.
2. Vorontsov I, Pillet S, Kaminski R, Schmokel MS, Coppens P (2010) LASER—a program for response-ratio refinement of time-resolved diffraction data. *J Appl Cryst* 43:1129–1130.
3. Adams PD, et al. (2010) PHENIX: A comprehensive Python-based system for macromolecular structure solution. *Acta Crystallogr D Biol Crystallogr* 66(Pt 2):213–221.
4. Terwilliger TC, Berendzen J (1996) Bayesian difference refinement. *Acta Crystallogr D Biol Crystallogr* 52(Pt 5):1004–1011.
5. Vosko SH, Wilk L, Nusair M (1980) Accurate spin-dependent electron liquid correlation energies for local spin-density calculations: A critical analysis. *Can J Phys* 58(8): 1200–1211.
6. Perdew JP (1986) Density-functional approximation for the correlation energy of the inhomogeneous electron gas. *Phys Rev B Condens Matter* 33(12):8822–8824.
7. Becke AD (1988) Density-functional exchange-energy approximation with correct asymptotic behavior. *Phys Rev A* 38(6):3098–3100.
8. Grimme S (2006) Semiempirical GGA-type density functional constructed with a long-range dispersion correction. *J Comput Chem* 27(15):1787–1799.
9. Schafer A, Horn H, Ahlrichs R (1992) Fully optimized contracted Gaussian-basis sets for atoms Li to Kr. *J Chem Phys* 97(4):2571–2577.
10. Lee CT, Yang WT, Parr RG (1988) Development of the Colle-Salvetti correlation-energy formula into a functional of the electron density. *Phys Rev B Condens Matter* 37(2):785–789.
11. Becke AD (1993) Density-functional thermochemistry. 3. The role of exact exchange. *J Chem Phys* 98(7):5648–5652.
12. Weigend F, Ahlrichs R (2005) Balanced basis sets of split valence, triple zeta valence and quadruple zeta valence quality for H to Rn: Design and assessment of accuracy. *Phys Chem Chem Phys* 7(18):3297–3305.
13. Klamt A, Schuurmann G (1993) Cosmo: A new approach to dielectric screening in solvents with explicit expressions for the screening energy and its gradient. *J Chem Soc Perk T* 2(5):799–805.
14. Ahlrichs R, Bar M, Haser M, Horn H, Kolmel C (1989) Electronic-structure calculations on workstation computers: The program system TURBOMOLE. *Chem Phys Lett* 162(3): 165–169.

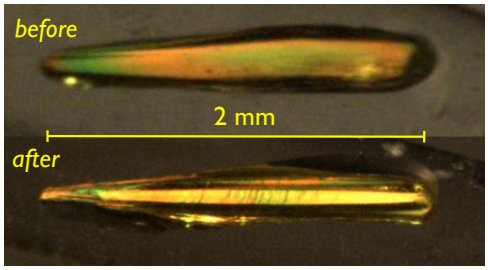

Fig. S1. Before and after photos of PYP7, one of nine crystals used to acquire time-resolved diffraction data. The crystal was viewed through crossed polarizers to suppress the background; variations in color are not real, but arise due to crystal birefringence. The "before" image appears homogeneous across its length. The image acquired after X-ray exposure reveals radiation-induced cracking of the crystal. These small cracks increase crystal mosaicity and reduce the diffraction quality. A total of 336 images were acquired from this crystal, i.e., 6 orientations with 56 time-resolved images acquired per orientation (including 12 interleaved −1-ns reference images).

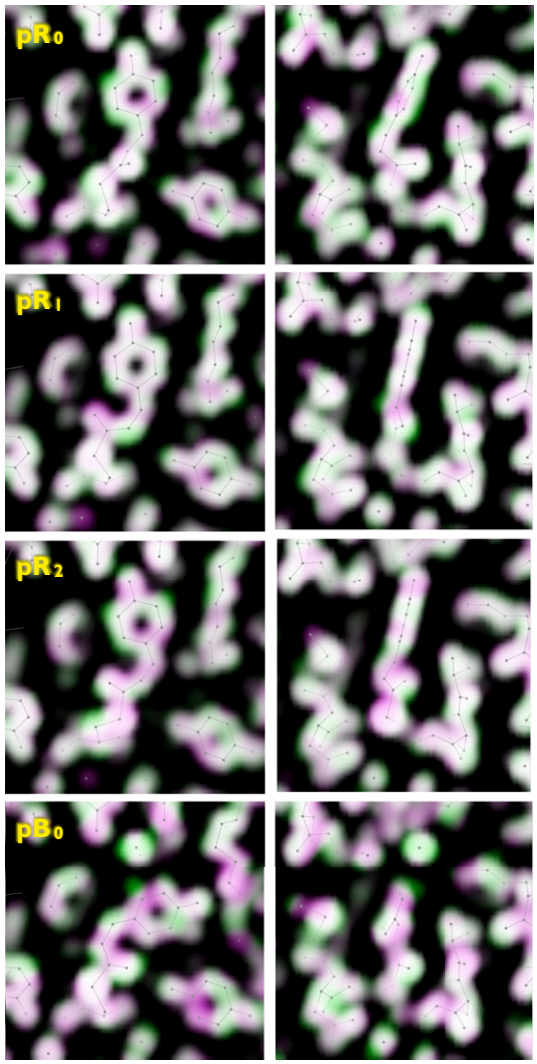

Fig. S2. Fit residuals are visualized via color-coded overlays of experimental (green) and calculated (magenta) electron density maps for pR_0, pR_1, pR_2, and pB_0 intermediates. The experimental maps were obtained by global analysis of the time-resolved structure-factor amplitudes. The calculated maps were generated from single structures refined against the experimental maps. The pastel coloration of the pCA electron density appears to vary randomly, demonstrating that the sequential kinetic model in Fig. 4*A* accounts for the time-dependent electron density changes with high fidelity.

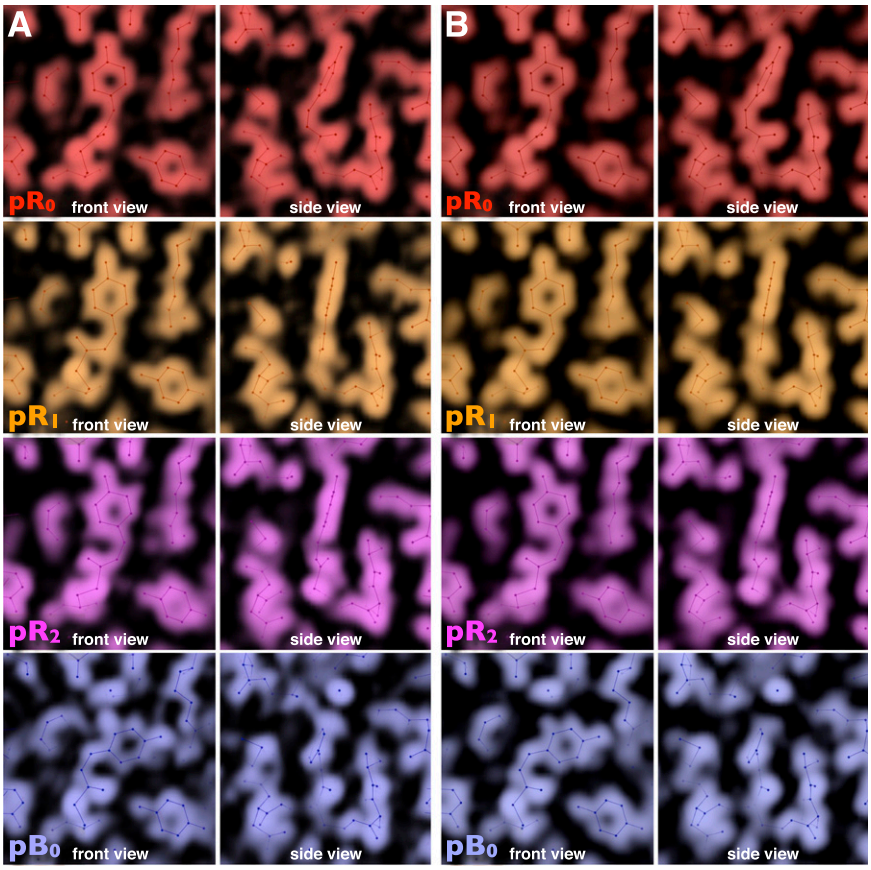

Fig. S3. Electron density maps of photocycle intermediates obtained by global analysis. (*A*) Calculated using phases from the ground state (pG) model for each of the four intermediates. (*B*) Calculated using refined phases from the model of each intermediate (same as in Fig. 4).

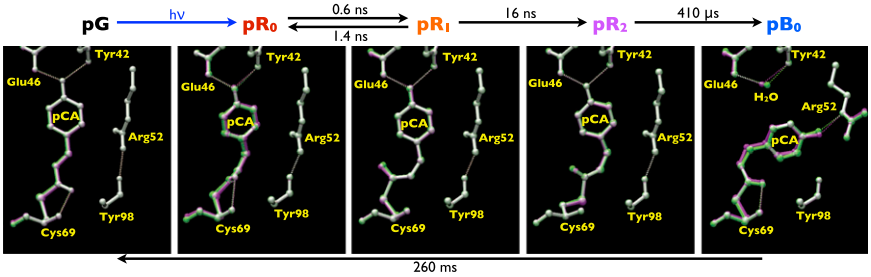

Fig. S4. Comparison of X-ray–refined (green) and DFT–optimized (magenta) structures. Where the structures overlap, they blend to white. For clarity, only the pCA and its hydrogen bonding partners are shown.

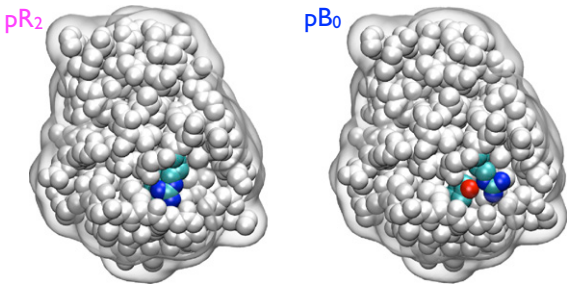

Fig. S5. During the pR_2-to-pB_0 transition, Arg52 swings from a closed to an open conformation, exposing the phenolate oxygen (red sphere) to water. This open conformation facilitates penetration of a water molecule into the pCA cavity, which is stabilized by hydrogen bonds with Tyr42 and Glu46, and likely prolongs the lifetime of the pB_0 state (rendered with VMD).

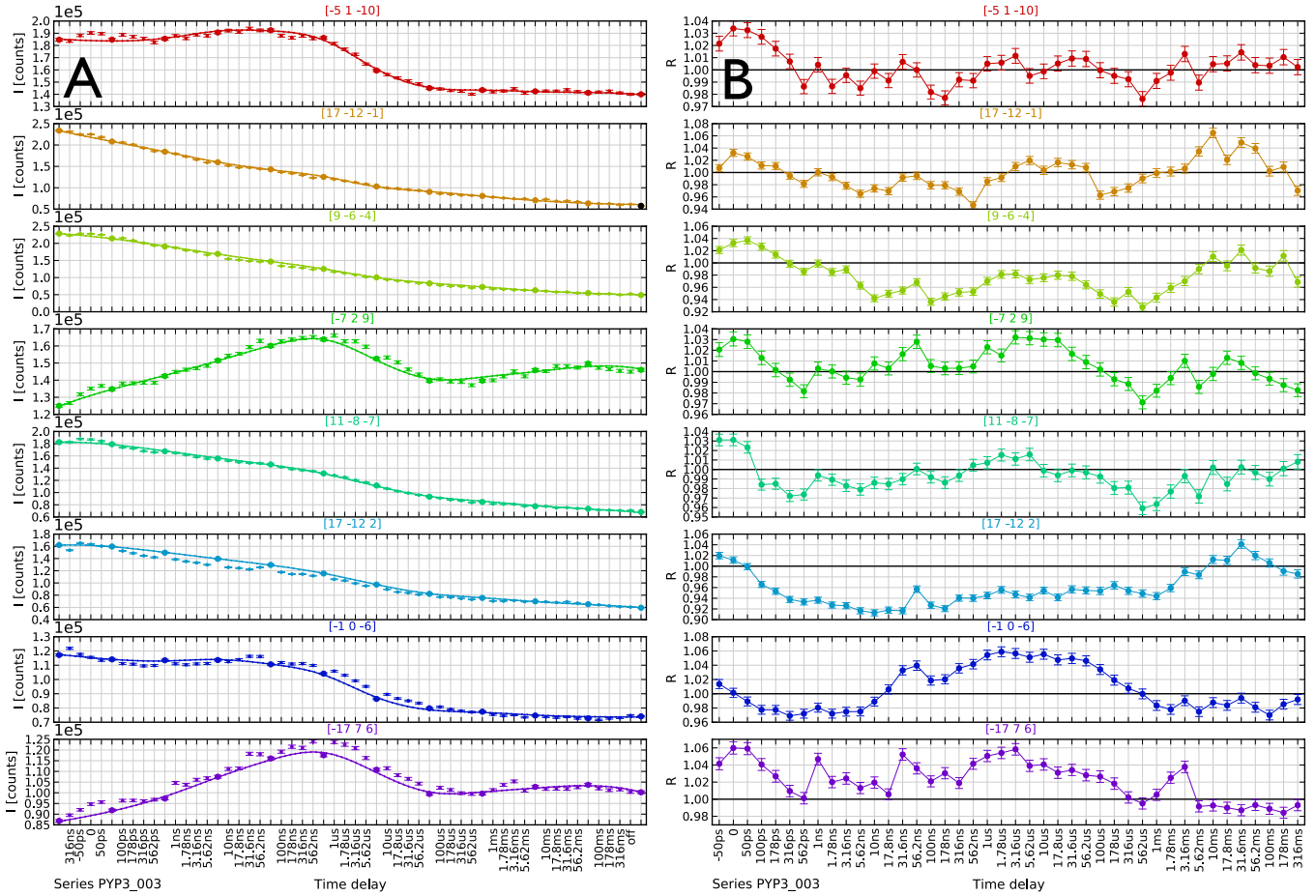

Fig. S6. Interpolated ratio method. (*A*) A cubic spline (solid line) interpolates between the integrated spot intensities in the reference images (−1-ns time points; large filled circles). The interpolated intensities are used to compute ratios, $R_{hkl} = I_t/I_{-1ns}$. The subset of reflections shown corresponds to the strongest indexed reflections found at a particular crystal orientation. Their integrated intensities (photons) have been normalized against I0, the relative X-ray intensity. The variation in intensity across the time series is due in part to crystal morphology, which leads to changes in the diffracting volume as the crystal is translated from one end to the other. (*B*) Time dependence of ratios calculated from data in *A*. Time-dependent changes in the protein structure cause some reflections to get brighter, and some dimmer.

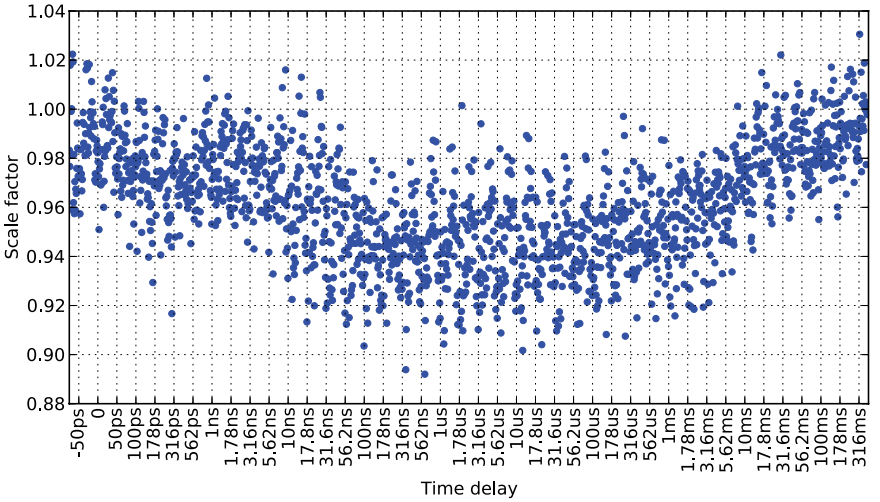

Fig. S7. Weighted average of R_{hkl} as a function of time delay for all 41 time series used in our structure analysis.

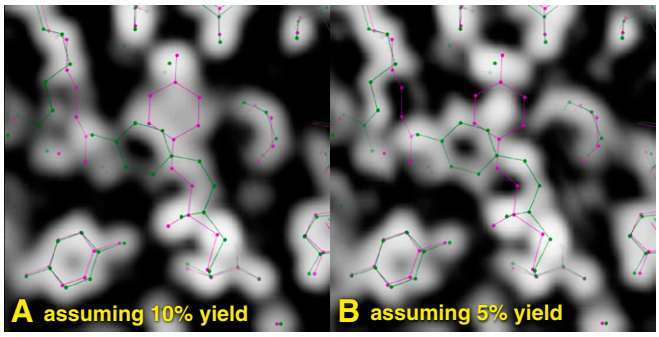

Fig. S8. Time-resolved electron density maps acquired 1 ms after photoexcitation (2 mF_O – DF_C; phased with ground-state model). The two maps were extrapolated to 100% population assuming a photoproduct yield of 10% (*A*) and 5% (*B*). Superimposed are ball-and-stick models of the pG ground state (magenta) and pB_0 state (green).

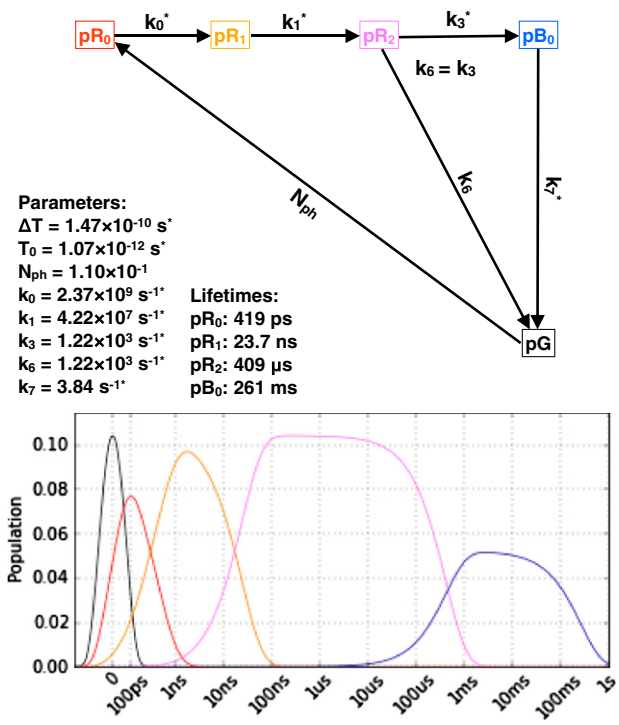

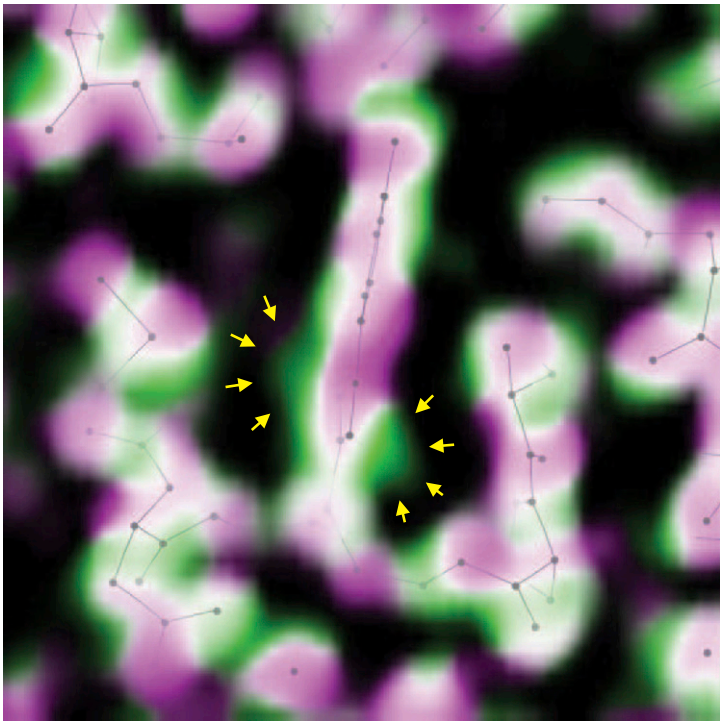

Fig. S9. (*Left*) Sequential kinetic model; refined parameters; and the corresponding population dynamics. (*Right*) Color-coded overlay of the pR_1 intermediate: atomic model density (magenta; F_O map phased with pR_1 model) and global analysis density (green; 2 mF_O – DF_C map phased with pR_1 model); ball-and-stick model of pR_1 state (gray). The excess green density highlighted by yellow arrows is found in the same location as the carbonyl oxygen in the pR_0 state, suggesting persistence of that state.

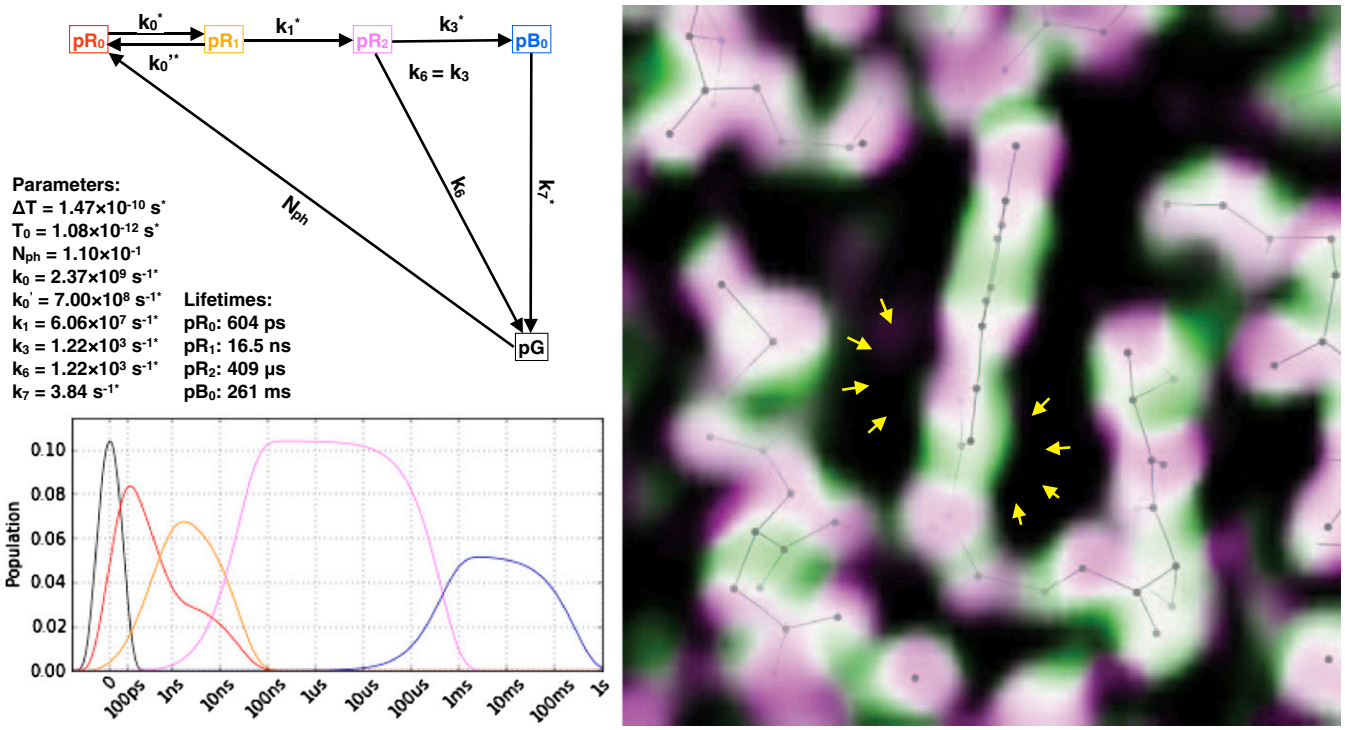

Fig. S10. (*Left*) Nonsequential kinetic model with equilibrium between pR_0 and pR_1; refined parameters; and the corresponding population dynamics. (*Right*) Color-coded overlay of the pR_1 intermediate: atomic model density (magenta; F_O map phased with pR_1 model) and global analysis density (green; 2 $mF_O - DF_C$ map phased with pR_1 model); ball-and-stick model of pR_1 state (gray). The electron density differences are modest, with little evidence for pR_0 contamination.

Table S1. Properties of each intermediate in the PYP photocycle

	pR_0	pR_1	pR_2	pB_0	pG
Lifetimes	600 ps	16 ns	410 us	260 ms	—
Stereochemistry					
Phe–C3=C2	27°	5°	16°	29°	7°
C1′–C3=C2–C1	*cis* (31°)	*cis* (–8°)	*cis* (2°)	*cis* (–1°)	*trans* (169°)
C3=C2–C1–S	*anti A*– (–152°)	*anti T* (174°)	*anti T* (175°)	*anti T* (155°)	*anti T* (169°)
C2–C1–S–Cβ	*anti A*– (–124°)	*syn C* (–24°)	*anti T* (–168°)	*anti T* (171°)	*anti T* (179°)
C1–S–Cβ–Cα	*syn G*– (–80°)	*syn G*- (–87°)	*anti A*+ (104°)	*syn G*– (–72°)	*syn G*- (–81°)
Hydrogen bonds					
pCA···Tyr42	2.54	2.57	2.47	—	2.51
pCA···Glu46	2.75	2.64	2.61	—	2.58
pCA···Cys69	3.04	—	—	2.91	2.82
pCA···Arg52	—	—	—	2.92	—
Cα··Cα distances					
Cys69–Tyr42	17.31	17.29	17.23	17.81	17.82
Cys69–Glu46	15.28	15.39	15.29	15.57	16.04
Cys69–Arg52	14.29	14.3	14.29	14.34	14.72
pCA S-O4 distance	8.30	8.62	8.67	8.28	9.05
DFT energies					
Total (relative to pG)	22.8	23.9	16.8	*	0
pCA···Tyr42	11.9	12.9	11.7	—	11.3
pCA···Glu46	8.3	9.5	10.2	—	10.9
pCA···Cys69	8.4	—	—	10.4	9.0
pCA···Arg52	—	—	—	10.7	—
pCA strain	16.1	10.6	6.2	5.7	4.9

Stereochemistry designations follow IUPAC convention. Hydrogen bond distances and other distances are given in Å. DFT energies are given in kcal·mol^{-1}. The pCA strain energy corresponds to the chromophore only. The shaded cells highlight configurations/distances that deviate significantly from pG.

*The energy of the pB_0 intermediate is not estimated because the particle number in its quantum chemical model is not conserved relative to pG.

Table S2. Crystallographic data and data collection statistics for the 41 time series used in our data analysis

Space group	P63
Unit cell a, b, c, Å	66.833, 66.833, 40.947
α, β, γ,°	90, 90, 120
Resolution, Å	13.3–1.60
Reflections (observed)	10,605
13.28–2.93 Å	1,756
2.93–2.32 Å	2,062
2.32–2.02 Å	2,078
2.02–1.84 Å	1,888
1.84–1.70 Å	1,675
1.70–1.60 Å	1,146
Reflections ($I/\sigma > 2$)	10,544
13.28–2.93 Å	1,753
2.93–2.32 Å	2,055
2.32–2.02 Å	2,072
2.02–1.84 Å	1,876
1.84–1.70 Å	1,662
1.70–1.60 Å	1,126
Completeness (observed)	0.76
13.28–2.93 Å	0.76
2.93–2.32 Å	0.89
2.32–2.02 Å	0.90
2.02–1.84 Å	0.81
1.84–1.70 Å	0.72
1.70–1.60 Å	0.49
Completeness ($I/\sigma > 2$)	0.76
13.28–2.93 Å	0.76
2.93–2.32 Å	0.89
2.32–2.02 Å	0.89
2.02–1.84 Å	0.81
1.84–1.70 Å	0.72
1.70–1.60 Å	0.49
Redundancy	5.11
13.28–2.93 Å	4.56
2.93–2.32 Å	6.09
2.32–2.02 Å	6.06
2.02–1.84 Å	5.69
1.84–1.70 Å	4.40
1.70–1.60 Å	2.56
$\langle I/\sigma_I \rangle$	34.5
13.28–2.93 Å	64.5
2.93–2.32 Å	57.2
2.32–2.02 Å	41.5
2.02–1.84 Å	25.2
1.84–1.70 Å	13.2
1.70–1.60 Å	5.4
R_{sym}	0.20
13.28–2.93 Å	0.12
2.93–2.32 Å	0.25
2.32–2.02 Å	0.22
2.02–1.84 Å	0.23
1.84–1.70 Å	0.21
1.70–1.60 Å	0.15

The structure factors observed are in common for all 42 time delays in each series (−50 ps, 0, 50 ps, +100 ps to 316 ms with four steps per decade). The signal-to-noise ratio does not change significantly across the time delays.

Table S3. Refinement statistics for each intermediate in the PYP photocycle

Intermediate	pR_0	pR_1	pR_2	pB_0
PDB ID code	4B9O	4BBT	4BBU	4BBV
R_{work}	0.221	0.169	0.165	0.255
R_{free}	0.308	0.228	0.218	0.360
No. of atoms	1,126	1,126	1,126	1,127
Protein	976	976	976	976
Water	139	139	139	140
Chromophore	11	11	11	11
B-factors, A^2	20.3	23.1	26.2	22.7
Protein, A^2	19	21.3	24.4	21.7
Water, A^2	30.2	36.2	39.2	30.2
Chromophore, A^2	11.1	15.7	19.6	15.8
Reflections ($I/\sigma_I > 2$)	7,038	8,171	8,940	6,948
13.28–2.93 Å	1,657	1,707	1,738	1,633
2.93–2.32 Å	1,724	1,877	1,962	1,699
2.32–2.02 Å	1,544	1,779	1,904	1,514
2.02–1.84 Å	1,151	1,405	1,579	1,108
1.84–1.70 Å	688	969	1,164	704
1.70–1.60 Å	274	434	593	290
Completeness ($I/\sigma_I > 2$)	0.51	0.59	0.64	0.50
13.28–2.93 Å	0.71	0.74	0.75	0.70
2.93–2.32 Å	0.74	0.81	0.85	0.73
2.32–2.02 Å	0.67	0.77	0.82	0.65
2.02–1.84 Å	0.50	0.61	0.68	0.48
1.84–1.70 Å	0.30	0.42	0.50	0.30
1.70–1.60 Å	0.12	0.19	0.26	0.13
$\langle I/\sigma_I \rangle$	4.6	6.9	11.6	5.1
13.28–2.93 Å	11.0	16.9	30.1	13.3
2.93–2.32 Å	6.9	10.6	17.7	7.7
2.32–2.02 Å	4.7	7.2	11.4	5.0
2.02–1.84 Å	2.7	4.0	6.1	2.7
1.84–1.70 Å	1.4	2.1	2.9	1.4
1.70–1.60 Å	0.7	0.9	1.2	0.6

The signal-to-noise ratio depends on the number of time points in which the intermediate is observed, and the yield with which it is generated.

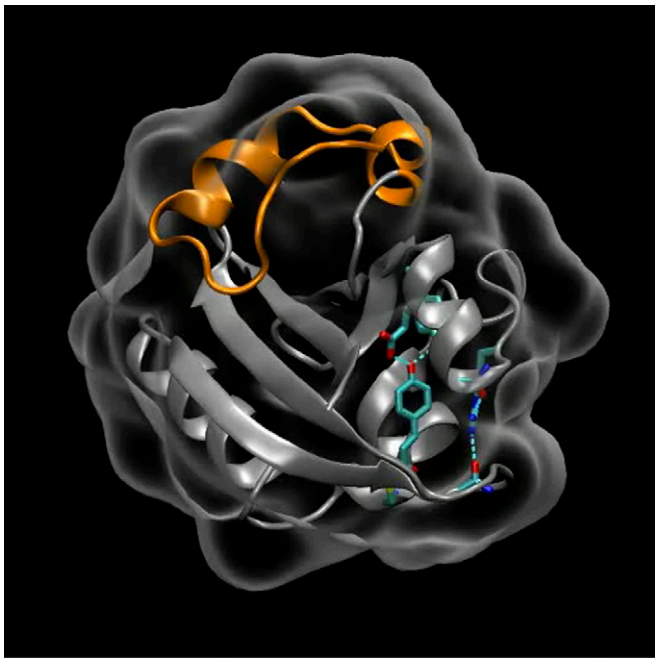

Movie S1. Ground-state structure of PYP. The backbone is rendered in ribbon with the N-terminal domain colored orange. The atoms rendered in licorice are colored according to type: C (cyan); N (blue); O (red); S (yellow). Relevant hydrogen bonds are indicated as dashed cyan lines (rendered with VMD).

Movie S1

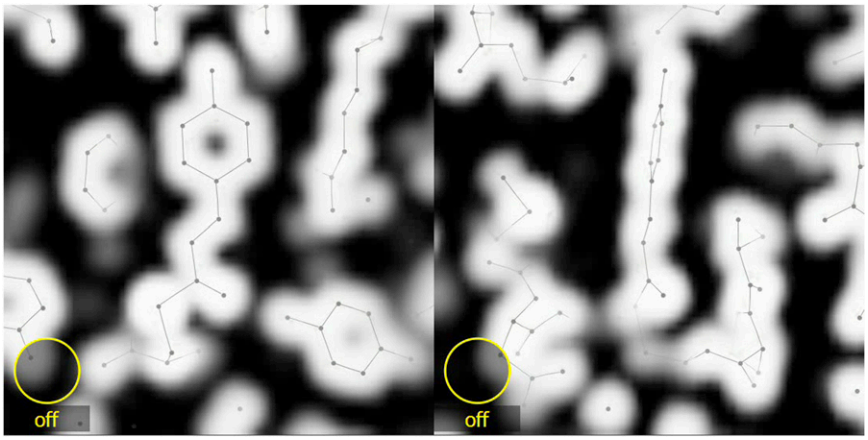

Movie S2. Time-dependent electron density maps spanning 10 decades of time. Both frontal and side views are shown. The ground state electron density maps are colored magenta, and the time-resolved maps are colored green. Where magenta and green overlap, the electron density blends to white. The magenta-to-green color gradient unveils the direction of atomic motion.

Movie S2

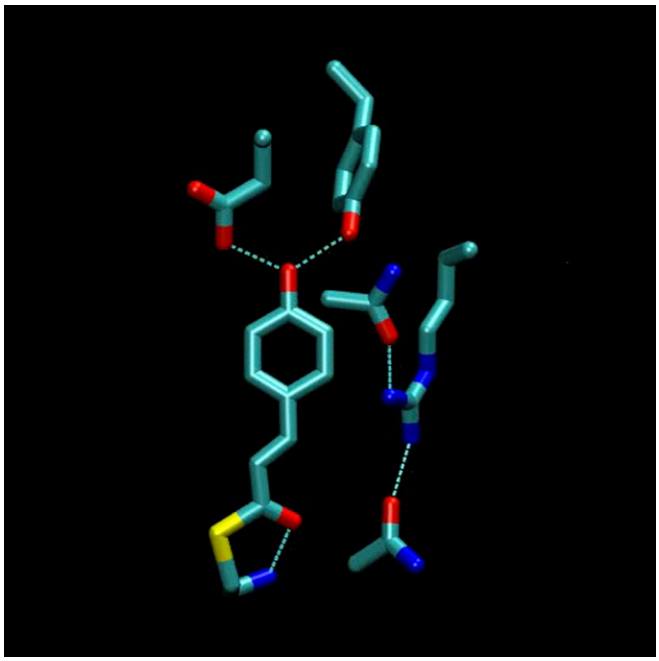

Movie S3. Color-coded rotating overlay of pCA structures and relevant side chains: pG (cyan); pR_0 (red); pR_1 (orange); pR_2 (magenta); and pB_0 (blue). After the first revolution, which shows pG only, overlaid structures before and after each successive transition are shown. This approach highlights the structural changes occurring during each transition. Water molecules are rendered as red spheres. Hydrogen bonds are rendered as dashed cyan lines (rendered with VMD).

Movie S3

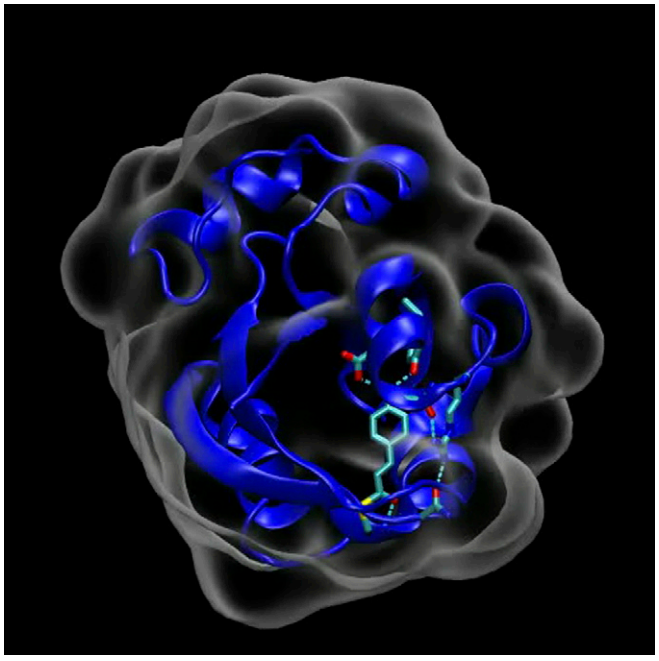

Movie S4. Color-coded structures of pG, pR_0, pR_1, pR_2, and pB_0, as in Fig. 4. The pCA and relevant side chains are colored cyan (pG), red (pR_0), orange (pR_1), magenta (pR_2), and blue (pB_0). Hydrogen bonds discussed in the main text are indicated as dashed cyan lines. The backbone is rendered blue-white-red according to atomic displacement relative to the pG state, with red in the color scale corresponding to 0.5 Å. The intermediate structure shown advances after each period in a rock-and-roll motion (rendered with VMD).

Movie S4